Boundary-Layer Meteorology (2005) 117: 479–510
DOI 10.1007/s10546-005-2188-2

SPECTRAL STRUCTURE OF SMALL-SCALE TURBULENT AND MESOSCALE FLUXES IN THE ATMOSPHERIC BOUNDARY LAYER OVER A THERMALLY INHOMOGENEOUS LAND SURFACE

MICHAIL A. STRUNIN[1] and TETSUYA HIYAMA[2,*]
[1]*Central Aerological Observatory, 3 Pervomayskaya St., Dolgoprudny, Moscow Region, 141700, Russia;* [2]*Hydrospheric Atmospheric Research Center (HyARC), Nagoya University, Nagoya, 464-8601, Japan*

(Received in final form 10 January 2005)

Abstract. Spectral analysis was performed on aircraft observations of a convective boundary layer (CBL) that developed over a thermally inhomogeneous, well-marked mesoscale land surface. The observations, part of the GAME-Siberia experiment, were recorded between April and June 2000 over the Lena River near Yakutsk City. A special integral parameter termed the 'reduced depth of the CBL' was used to scale the height of the mixed layer with variable depth. Analysis of wavelet cospectra and spectra facilitated the separation of fluxes and other variables into small-scale turbulent fluctuations (with scales less than the reduced depth of the CBL, approximately 2 km) and mesoscale fluctuations (up to 20 km). This separation approach allows for independent exploration of the scales. Analyses showed that vertical distributions obeyed different laws for small-scale fluxes and mesoscale fluxes (of sensible heat, water vapour, momentum and carbon dioxide) and for other variables (wind speed and air temperature fluctuations, coherence and degree of anisotropy). Vertical profiles of small-scale turbulent fluxes showed a strong decay that differed from generally accepted similarity models for the CBL. Vertical profiles of mesoscale fluxes and other variables clearly showed sharp inflections at the same relative (with respect to the reduced depth of the CBL) height of approximately 0.55 in the CBL. Conventional similarity models for sensible heat fluxes describe both small-scale turbulent and mesoscale flows. The present results suggest that mesoscale motions that reach up to the relative level of 0.55 could be initiated by thermal surface heterogeneity. Entrainment between the upper part of the CBL and the free atmosphere may cause mesoscale motions in that region of the CBL.

Keywords: Aircraft observation, Inhomogeneous land surface, Turbulent and mesoscale characteristics, Wavelet transform.

I. Introduction

Determining the roles of small-scale chaotic fluctuations in velocity components (turbulence) and larger-scale motions (coherent structures, large thermal plumes) is fundamental to understanding exchange processes in the atmospheric boundary layer (ABL). The structure and magnitude of sensible

* E-mail: hiyama@hyarc.nagoya-u.ac.jp

heat and water vapour fluxes in the ABL, and fluxes of passive substances (such as carbon dioxide), depend strongly on the scale of eddies moving the substances. Heterogeneous land surfaces strongly affect the structure of the convective boundary layer (CBL), and characteristics of this influence depend on typical scales of surface heterogeneity.

One approach to specifying the scales is to use Raupach's length L_{Rau} to determine the application of different CBL parameterisations (Mahrt, 2000):

$$L_{\mathrm{Rau}} = C_{\mathrm{Rau}} \frac{U z_i}{w_*}, \tag{1}$$

where z_i is the depth of the CBL and w_* is the convective or Deardorff velocity (Deardorff, 1970), U is the mean wind speed and $C_{\mathrm{Rau}} \approx 0.8$ is a non-dimensional factor determined from observations. L_{Rau} is applicable to the convective boundary layer, and can be compared to the surface heterogeneity scale L_{hetero}; if $L_{\mathrm{hetero}} < L_{\mathrm{Rau}}$, similarity models can be used to predict flux distributions. This situation corresponds to microscale heterogeneity. The ratio$L_{\mathrm{Rau}}/L_{\mathrm{hetero}}$ is therefore an essential criterion determining the applicability of scaling models, and the ratio was used successfully in a procedure separating subgrid areas using flux aggregation or the mosaic approach (Strunin et al., 2004).

Other cases exist wherein $L_{\mathrm{Rau}} < L_{\mathrm{hetero}} < T_{\mathrm{E}}U$, where T_{E} is an entrainment time scale. The CBL usually develops in 2 or 3 h during the morning, and the entrainment length scale $T_{\mathrm{E}}U$ for typical wind speeds of 3–5 m s^{-1}, and for a time scale of 2–3 h, is more than 30–40 km. This length scale corresponds to mesoscale heterogeneity, which is a typical situation as the summer CBL develops over a surface that includes relatively cold patches with scales between 5 and 20 km (small lakes, rivers or swamps). According to Mahrt (2000), no rigorous solution exists for situations with mesoscale heterogeneity.

Another approach separates CBL flow into small-scale turbulent and mesoscale parts that are then analysed independently. Kaimal (1978) considered the low frequency and high frequency parts of the horizontal wind speed spectra separately. The boundary between low- and high-frequency portions of spectra equated to the frequency that corresponded to the CBL height. Hojstrup (1982) suggested different scalings for the low- and high-frequency parts of the horizontal wind speed spectra. Chaotic eddies with sizes less than the depth of the CBL (typically 1–2 km) are characterised as small-scale turbulence. Flows in the CBL with scales that exceed the depth of the layer (i.e., mesoscale motions with scales from 1–2 km up to 20 km) should behave differently.

Spectral analysis based on a wavelet transform allows scale separation, and a particular advantage of wavelet transform is that it allows analysis of inhomogeneous signals. Attie and Durand (2003) used conventional wavelet transforms to study the heterogeneous structure of a thermal internal boundary layer associated with a sea-breeze circulation. They estimated the contributions of turbulence to the vertical sensible heat flux at different scales and linked surface inhomogeneities to characteristics of the fluxes.

Observations for the present study were made as part of the Global Energy and Water Cycle Experiment (GEWEX) Asian Monsoon Experiment-Siberia (GAME-Siberia) project. Aircraft observations during the intensive observation period from April to June 2000 (IOP2000) were made near Yakutsk City in eastern Siberia. Previous analyses revealed the development of a mesoscale thermal internal boundary layer (MTIBL) inside the CBL over the Lena River and its banks (Strunin et al., 2004). The CBL had an inhomogeneous structure, and the local depth of the CBL varied significantly. In addition, a local circulation developed over the Lena River. Strong temperature differences between the riverbanks and the relatively cold river forced this localised circulation over upwind riverbanks (Hiyama et al., personal communication, 2004). The local circulation supported horizontal and vertical fluxes at scales that exceeded the depth of the CBL.

This study sought to determine, model, and parameterise fluxes of momentum, sensible heat, water vapour, and carbon dioxide. The fluxes are representative of those in a convective boundary layer developing over thermally inhomogeneous land surfaces. Wavelet spectral analyses of fluxes will help define how different-sized eddies contribute to energy, water vapour, and carbon dioxide transport throughout the CBL.

2. Aircraft Observations and Methods of Analysis

Hiyama et al. (2003) detailed the aircraft observations during the IOP2000 near Yakutsk City. The present study used data from research flights in 2000 at approximately 1-week intervals, depending on weather conditions, on May 1, 9, 12, and 20, and on June 1, 5, 9, and 19.

2.1. Aircraft instruments

A Russian-built ILYUSHIN-18 aircraft carried instruments to measure atmospheric variables and flight parameters during the intensive observation period (IOP); Strunin (1997) and Strunin and Hiyama (2004b) provide details of the aircraft instruments. The aircraft recorded the following variables:

- Flight parameters, i.e., current barometric aircraft height h_b, airspeed of aircraft V, heading angle φ, position by geographic coordinates latitude 'Lat' and longitude 'Lon'.
- Thermodynamic atmospheric conditions, i.e., air temperature T, mean wind speed U, wind direction ψ.

- Fluctuations in vertical w' and horizontal (longitudinal with respect to the flight direction) u' components of wind speed, air temperature T' and absolute air humidity q', and carbon dioxide density C'.
- Surface conditions and infrared surface temperature T_s.

A global positioning system (GPS) tracked the aircraft position (longitude and latitude) with an error of less than 100 m, and an onboard barometer measured the flight level with an accuracy of 10 m. The aircraft navigation system measured the heading angle φ with an error of less than 1°; aircraft speed was measured with an accuracy of about 0.2 m s^{-1}. Root-mean-square errors of air temperature T and wind speed U measurements were 0.4 K and 0.4 m s^{-1}, respectively; the measurement error of wind speed direction did not exceed 5°.

Several sensors comprised the gust-probe system that measured atmospheric turbulence; a high-response pressure sensor, connected to a Pitot pressure probe and static pressure holes, measured dynamic pressure. A barometer, connected to the static pressure holes of the aircraft pressure system, measured static pressure; a high-response platinum wire thermometer, specially designed for aircraft conditions, measured air temperature. Measured pressure differences in the holes of a spherical probe helped to determine the angle of attack. Gyros measured variations in pitch angle, and a stable accelerometer measured variations in vertical acceleration. A Doppler radar measured the horizontal components of the aircraft's ground speed; the vertical component of the aircraft's ground speed was determined by integrating aircraft accelerations. Vertical and horizontal wind speed fluctuations and air temperature fluctuations were calculated using well-known gas-dynamics equations (Lenschow, 1972).

Turbulence observations were made only along flight paths with no acceleration or altitude changes; such flight paths were termed sampling legs. Atmospheric turbulence disturbed the aircraft's motion on sampling legs at lower levels, but variability in aircraft speed did not exceed 1.4 m s^{-1}. Changes in flight level did not exceed 20 m and variations in heading and roll angles did not exceed 5°. Measurement accuracies for the wind speed and temperature fluctuations were about 8%, or 0.1 m s^{-1} and 0.02 K, respectively.

An ultraviolet hygrometer (Lyman-α sensor) designed at the Central Aerological Observatory (Mezrin, 1997) measured absolute air humidity fluctuations q' with a time constant of 0.1 s and an accuracy of 0.02 g kg^{-1} (in specific humidity). The density and fluctuations of carbon dioxide were measured with a fast-response CO_2/H_2O gas analyser (LI-6262, Li-COR, U.S.A.). A downward-pointed infrared radiometer/thermometer (model 4000-4GL, Everest, U.S.A.) incorporated simple atmospheric corrections to measure the temperature of the underlying surface.

All data were recorded at a frequency of 20 Hz on an onboard computer. Special processing validated data, checked errors, and stored information in the database files.

2.2. SAMPLING SITE AND MEASUREMENTS

The sampling site near Yakutsk included two riverbanks of the Lena River. Long flight paths between the banks crossed the Lena River lowlands at an angle nearly perpendicular to the main river channel. These regional flight paths, each about 90 km long in the east–west direction, were made at five different levels above the highest point of the underlying terrain. Figure 1 includes maps of sampling sites and vertical profiles of the terrain under the regional flight paths. The heading angle φ equals 118° at flight levels of 100, 300 and 1500 m; φ equals 298° at flight levels of 150 and 800 m. Measurements along the regional flight paths were recorded between 1200 and 1330 local solar time. This is the time of the day when temporal variations in surface fluxes should not be large. Data collection began only if clouds covered less than 50% of the sky, rainfall was absent, and winds were at most 15 m s^{-1}. Although flights began under these conditions, clouds that capped the CBL sometimes developed and overspread the sky during the flight.

Each research flight followed the same flight path (to within 100 m) and time schedule (to within 5–10 min). Vertical aircraft soundings of the ABL over the Lena River from 100 m up to 4000 m over the left bank and from 4000 m down to 100 m over the right bank were taken immediately after regional flight measurements. Two ground stations, 'Spasskaya Pad' and 'Ulakhan Sykkan,' provided data under the regional paths, but these two stations could not characterise general conditions of the heterogeneous land surface out to 90 km.

The surface under the flight paths was inhomogeneous. Terrain included small hills (terraces) covered with forests (mainly larch, pine and birch), grassy fields, and small lakes. Lena River lowlands, surrounded by bluffs, comprised the central part of the surface under the regional paths. The lowlands included the main channel and many branches of the river. The surface state and the state of the Lena varied with the seasons. Similarly, the size of the heterogeneous underlying surface and the temperature contrast between the river lowland and the surrounding terrace also changed with the season. Infrared surface temperatures measured from the lowest flight level (100 m) reflected seasonal variations in surface heterogeneity.

Table I presents the main variables, averaged in 100-m segments along the 90-km regional flight paths, for each of the aircraft observation days. Estimated ABL depths were large: more than 1500 m in most cases. This result suggests that the top of the surface layer should have been at approximately 100–150 m, and measurements at the 100-m flight level were probably in the

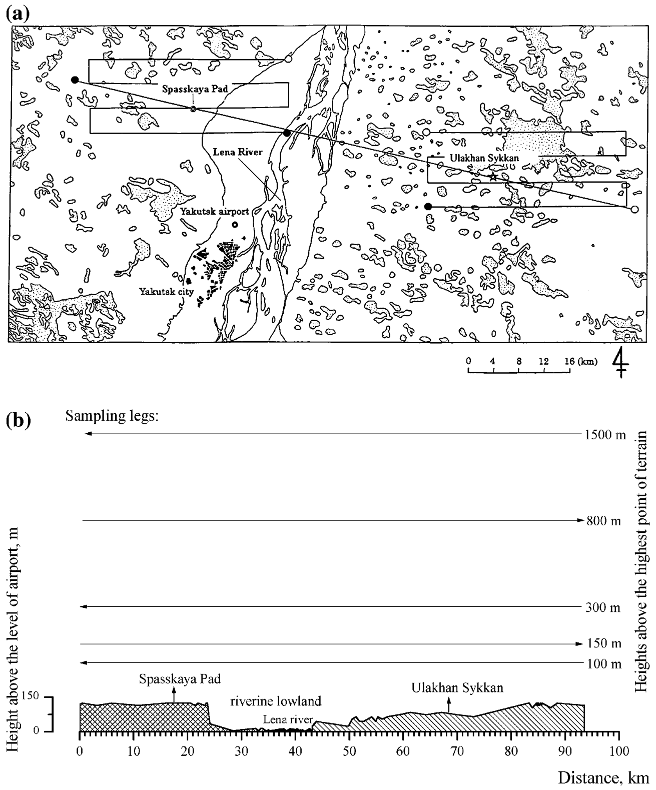

Figure 1. (a) Map of the sampling area in the vicinity of Yakutsk city including the scheme of aircraft observations. Shaded areas on the forested terraces indicate grass fields (clearings). Lena riverine low land, on which Yakutsk city are located, is mostly occupied by grass fields also. Open and solid circles are starting and ending points of each flight scheme. Observation sites for the ground-based tower measurements over a larch and a pine forest sites ('Spasskaya Pad' marked as ◎) and those over a grass field ('Ulakhan Sykkan' marked as ☆) were located directly under the regional flight paths. (b) Landscape profile under the regional sampling legs and schemes of flights levels.

upper part of the surface layer. Radiosonde data reported in Strunin et al. (2004) support this contention. Continuous measurements of temperature and humidity during aircraft soundings yield estimates of ABL depth and atmospheric stability. Vertical potential temperature profiles (Figure 3 in Strunin et al., 2004) suggest that the ABL over the sampling area was convective during all observation days. In addition, the stability parameter $\frac{z}{L}$ (where z is the height above the surface and L is Obukhov's length) estimated at the 100-m level of the regional flight paths was consistent with boundary-layer instability. Table I shows that $\frac{z}{L}$ varied from -0.6 (weak unstable conditions) to -10 (strong unstable conditions). Table I also includes estimates of the main CBL depth z_i.

TABLE I

Parameters of the CBL over the banks and riverine lowland of the Lena River.

Date parameter	May 1	May 9	May 12	May 20	June 1	June 5	June 9	June 19
Existence of MTIBL	No	No	No	Yes	No	Yes	Yes	Yes
z_i, m	1700	1800	1900	2500	2700	2200	3000	3200
δ_i, m	1700	1600	1900	2200	2700	1500	1600	1400
U, m s^{-1}	6.1	2.9	9.5	2.8	8.0	3.4	4.5	1.9
ψ, °	303	245	158	108	318	74	229	219
L_{hetero}, m	6000	7000	3000	11000	11000	11000	11000	12000
L_{Rau}, m	4000	2300	6100	2700	6700	3100	4200	2200
$\frac{z}{L}$	−0.6	−1.6	−2.2	−2.1	−0.6	−6.2	−2.2	−10.1
T_s, ° C	5.3	10.6	20.0	16.8	22.0	23.8	30.8	30.6
$M_{\max}$, 10^{-2} N m^{-2}	−66.5	−27.6	−54.5	−17.9	−83.9	−15.1	−26.3	−8.3
H_0, W m^{-2}	186.8	119.1	233.4	122.3	229.2	118.8	174.9	121.0
$E_{\max}$, mg m^{-2} s^{-1}	19.10	19.74	58.33	50.24	40.58	54.45	114.86	59.93
$\lvert Q_{\max}\rvert$, mg m^{-2} s^{-1}	0.849	0.777	2.762	0.685	0.608	0.702	0.544	0.607

z_i: depth of the CBL defined from vertical soundings; δ_i: reduce value of the CBL depth; U: line-averaged wind speed at 100-m flight level; ψ: line-averaged wind direction; L_{hetero}: estimated maximum horizontal scale of surface heterogeneity; L_{Rau}: Raupach's length; $\frac{z}{L}$: atmospheric stability at 100-m flight level; T_s: line-averaged surface temperature; $M_{\max}$: line-averaged maximum (in absolute value) momentum flux; H_0: line-averaged sensible heat flux at 100-m flight level; $E_{\max}$: line-averaged maximum water vapour flux; $\lvert Q_{\max}\rvert$: absolute value of line-averaged carbon dioxide flux.

T_s data from the lowest flight level were used to minimise errors introduced by infrared radiation from the underlying air mass and to increase the resolution of the thermal heterogeneity of the underlying surface; T_s values in Table I are also line-averaged. Continuous measurements of infrared surface temperature T_s at 100 m yielded estimates of the horizontal scale of surface heterogeneity L_{hetero}. Fourier power spectra of T_s were calculated and scales that corresponded to the first and largest peaks of the spectra were used as surface heterogeneity scales L_{hetero}. A χ^2-distribution (Vinnichenko et al., 1980) yielded estimates of the stability of the surface temperature power spectra and L_{hetero} error at 1 km. The maximum sampling path was 90 km. Windowed Fourier analyses suggest that corrections and reliable estimates of power spectra can be made only for scales less than 10% of the sampling distance, or less than 9–10 km. However, some surface thermal features with scales exceeding 9–10 km had large amplitudes and were clearly evident in the T_s data. Thus, large-scale heterogeneity L_{hetero} could be estimated directly from T_s datasets as a temperature anomaly.

In general, because surface features that comprise the surface heterogeneity are not isotropic, the associated length scale L_{hetero} depends on the measurement direction. The surface heterogeneity scale most relevant to the development of the internal boundary layer should be taken along the wind direction. The main surface feature near Yakutsk City that controls land surface heterogeneity is the Lena River and the surrounding forest. During the spring, when the measurements were made, water flooded most of the Lena River lowlands and horizontal scales of surface features did not depend on measurement direction. The earliest observations (May 1) were made when the Lena River was ice-covered. Nevertheless, a very narrow wind direction range can be identified for which L_{hetero} may be much larger. Such a wind direction is along the Lena River with $\psi = 20°$ to $40°$ or $\psi = 200°$ to $220°$ (see Figure 1). Table I shows that such wind directions were not observed in most cases. All flights were across the river, so estimates of L_{hetero} were minimum scales.

Table I provides estimates of Raupach's length L_{Rau} calculated using (1) for the 90-km regional flight path at 100 m.

2.3. Data processing techniques

2.3.1. *Flux Calculations and Scaling Parameters*

Eddy correlation methods were used to calculate vertical sensible heat fluxes:

$$H = c_p \rho \overline{w'\theta'}. \tag{2}$$

Here, θ' is the potential temperature fluctuation, c_p is the specific heat of air, and ρ is the air density; H is positive upward. Vertical fluxes of momentum, water vapour, and carbon dioxide were calculated using

$$M = \rho \overline{u'w'}, \tag{3}$$

$$E = \overline{w'q'}, \tag{4}$$

and

$$Q = \overline{w'C'}, \tag{5}$$

respectively. Overbars in (2)–(5) denote spatial (along the flight path) means (in the turbulent sense); primes denote turbulent fluctuations. The velocity scale (convective velocity) was obtained as (Deardorff, 1970):

$$w_* = \left(\frac{g H_{v0}}{\rho c_p \theta_{v0}} \delta_i \right)^{1/3}. \tag{6}$$

The temperature scale (convective temperature) was obtained from

$$\theta_* = \frac{H_{v0}}{\rho c_p w_*}. \tag{7}$$

$H_{v0} = H_0 + c_p T_0 E_0$ is the buoyancy flux estimated from the usual approximations (Brutsaert, 1982). The subscript '0' refers to the 100-m flight level, and θ_{v0} is virtual potential temperature, T_0 is the mean temperature, E_0 is the water vapour flux, g is the gravitational acceleration and δ_i is a vertical length scale of the CBL.

The depth of the CBL z_i is usually applied as a vertical scale above the surface layer. Vertical aircraft soundings up to 4 km made in the middle of the day over the left and right banks of the Lena River yielded estimates of z_i over the sampling site on different IOP days (see Figure 3 in Strunin et al., 2004). Temperature profiles in the upper part of the boundary layer were nearly adiabatic. A strong temperature inversion indicated the top of the CBL. Operational radiosondes from Yakutsk City confirmed estimates of z_i in Table I. Vertical profiles of specific humidity also support the CBL depth estimates. Temperature and humidity profiles from aircraft and radiosonde agreed at all levels. Visual estimates from the aircraft of cloud-base heights over the banks corroborated z_i estimates.

A mesoscale thermal internal boundary layer (MTIBL) was observed during some of the aircraft flights, and the MTIBL radically changed the CBL structure (Strunin et al., 2004). MTIBL development was apparent as a local decrease of the top of the CBL over the Lena River and its lowlands (cold patches on the land surface). Unstable conditions over the river banks determined z_i and could not characterise correctly the vertical scale of the CBL that developed over a heterogeneous land surface. A local depth of the CBL $\delta(x)$, defined as a function of distance along the regional flight path x, successfully modelled the non-homogeneous CBL using the mosaic or flux aggregation approach (see Figures 4–6 in Strunin et al., 2004). Evaluations of $\delta(x)$ were based on vertical cross-sections of buoyancy fluxes H_v accumulated along the regional flight path. The requirement for the $\delta(x)$ estimates was that the buoyancy flux was zero at the top of the boundary layer. This is a typical CBL characteristic over a homogeneous surface (e.g., Stull, 1988; Kaimal and Finnigan, 1994). To characterise the vertical scale in the CBL over a heterogeneous land surface, the reduced value δ_i of the CBL depth is defined as the integral parameter

$$\delta_i = \frac{1}{L_{\max}} \int_0^{L_{\max}} \delta(x)\, dx, \tag{8}$$

where $L_{\max}$ is the total regional flight path distance. Estimates in the present study suggest that the error in δ_i did not exceed 100 m. Table I also shows reduced depths δ_i for different flight days. Differences between z_i and δ_i were significant only if an MTIBL developed and the top of the CBL decreased over a cold patch. Values of δ_i were used instead of the main depth of the CBL z_i in scaling equations, and all scaling profiles were constructed relative to the normalised (or relative) height $\frac{z}{\delta_i}$ (z is the height above the underlying surface).

An equation based on Wyngaard (1973) and Lenschow et al. (1994) estimates the random sampling error in the flux computations. For this calculation, integral scales were evaluated using the empirical expression in Lenschow and Stankov (1986). The long sampling path length (more than 90 km) constrained the estimated random sampling error to less than 25% for all fluxes.

Systematic errors in the flux measurements were evaluated using an equation from Mann and Lenschow (1994). Eulerian integral length scales in the equation were defined with wavelet cospectra (via the wavelet transform as described below). Because the total sampling path length was large (more than 90 km), systematic flux errors were negligibly small (less than 1%).

2.3.2. *Spectral (Wavelet) Analysis*

A wavelet transform was applied to yield a spectral analysis of the turbulent variables $f(t)$ or $g(t)$ and turbulent fluxes in the CBL. A detailed description and investigation of this method is presented in Strunin and Hiyama (2004a). The basis function ('mother' wavelet) used was the Morlet wavelet (Grossman and Morlet, 1984),

$$\Psi(t) = \frac{1}{\pi^{1/4}} (\cos \omega_0 t + i \sin \omega_0 t)\, e^{-t^2/2}, \tag{9}$$

where the non-dimensional frequency $\omega_0 = 6$ represents the optimal value that yielded good time localisation and frequency resolution. The Morlet wavelet is a commonly used mother wavelet for studying turbulence, because it is suitable both for statistical analyses such as variance and covariance analysis and for pattern recognition of different turbulence events (Walker, 1997).

The Fourier transform of the Morlet basis wavelet is (Kumar and Foufoula-Georgiou, 1994)

$$\Psi^*(\omega) = \pi^{-1/4}\, e^{-(\omega-\omega_0)^2/2}. \tag{10}$$

The normalising coefficient C_Ψ used for spectral calculations was defined according to (Kumar and Foufoula-Georgiou, 1994):

$$C_\Psi = 2\pi \int_0^\infty \frac{|\Psi^*(\omega)|^2}{\omega}\, d\omega. \tag{11}$$

With $\omega_0 = 6$, numerical integration gives $C_\Psi = 1.0636$.

Turbulence characteristics derived from aircraft turbulence data are usually calculated using length a and wavenumber k. Taylor's hypothesis converted time t to distance b as $b = Ut$, and frequency ξ to wavenumber k as $k = \frac{\xi}{U}$. The wavelet transform was applied to a spatial-scale function $f(x)$ as follows:

$$Wf(a,b) = \frac{1}{|a|^{1/2}} \int_{-\infty}^{+\infty} f(x) \Psi\left(\frac{x-b}{a}\right) dx, \tag{12}$$

where $a = \frac{1}{k}$ is the spatial scale of the turbulent eddy, and b is the distance along the flight path (or location). Two matrices with coefficients from the real and imaginary parts of the wavelet transform were obtained by applying (10). Matrices of $|Wf(a,b)|^2$ values were calculated and defined as the wavelet scalogram of function $f(x)$ (Flandrin, 1988). The wavelet spectrum was calculated as (Hudgins et al., 1993)

$$S_f(a) = C_\Psi^{-1} \int_{-\infty}^{+\infty} |Wf(a,b)|^2 db. \tag{13}$$

Wavelet coefficient matrices for different turbulent variables (such as vertical and horizontal wind speed, air temperature, humidity and carbon dioxide density fluctuations) were used for calculating a cross-scalogram of $Wf(a,b)\overline{Wg(a,b)}$ and a wavelet cross-spectrum (Hudgins et al., 1993) as follows:

$$S_{fg}(a) = C_\Psi^{-1} \int_{-\infty}^{+\infty} Wf(a,b)\overline{Wg(a,b)} db, \tag{14}$$

where $\overline{Wg(a,b)}$ is the complex conjugate wavelet transform of the random function $g(x)$.

Real and imaginary parts of a cross-spectrum were used as the wavelet cospectrum $Co_{fg}(a)$ and quadrature spectrum $Qu_{fg}(a)$, respectively (Lui, 1994). Integrating the cospectra provides the corresponding flux for a selected scale range (from scale a_1 to scale a_2):

$$Q_{fg} = K_F \int_{a_1}^{a_2} Co_{fg}(a)\, da, \tag{15}$$

where $K_F = c_p\ \rho$ for the sensible heat flux, $K_F = \rho$ for the momentum flux and $K_F = 1$ for others (see (2)–(5)).

A wavelet square spectrum of coherence was calculated using (Lui, 1994)

$$Ch_{fg}^2(a) = \frac{|Co_{fg}(a)|^2 + |Qu_{fg}(a)|^2}{S_f(a)S_g(a)}. \tag{16}$$

Past studies demonstrated the reliability of the wavelet method using the present dataset (Strunin and Hiyama, 2004a). Good coincidence of the Morlet wavelet with the Fourier spectra for small-scale turbulent eddies has been shown; comparisons of Morlet and Haar wavelet spectra have also shown good results for most spectra. Covariances, defined through Morlet cospectra, were practically coincident with fluxes, as determined by calculations based on Equations (2)–(5). Variances calculated from the spectra agreed with direct calculations. Differences did not exceed 2%, implying that the wavelet method overlapped all scale ranges for the fluctuations investigated (Strunin and Hiyama, 2004a).

3. Results

MTIBLs occurred within the CBL on several experiment days (see Table I). The MTIBL developed under unstable thermal conditions above strong thermal surface features (Strunin et al., 2004) and radically altered the CBL structure. Effects from the Lena River also caused a local circulation over the riverbanks (personal communication). Thus, a combination of small-scale turbulent and mesoscale motions likely determined the inhomogeneous structure of the CBL.

The CBL started to develop in early morning and grew rapidly during the three hours prior to noon. The entrainment length scale $T_E U$ of CBL development for the different flight days was 20–100 km given the 3-h time scale. Comparisons between typical scales of L_{hetero} (surface heterogeneity) and L_{Rau} (Raupach's length) show uncertain situations ($L_{\mathrm{Rau}} < L_{\mathrm{hetero}} < T_E U$) on all experimental days except May 12. The uncertainty means no rigorous simulation model exists for scaling fluxes (see Mahrt, 2000). One way to solve the problem is to apply different similarity models to the small-scale turbulent and mesoscale portions of the cospectra.

3.1. Wavelet cross-scalograms

Wavelet cross-scalograms, which are the real parts of matrixes $Ww(a,b)\overline{W\theta(a,b)}$ and $Ww(a,b)\overline{WC(a,b)}$ (see (14)), were an intermediate result of spectral processing. These cross-scalograms represent flux distributions for wavenumbers and distance along the regional flight path (see Figure 2 for $Ww(a,b)\overline{W\theta(a,b)}$). Each panel contains contours of cross-scalograms; the logarithm of eddy wavelength is the ordinate, and distance along the flight path is the abscissa. It is therefore possible to identify events in flux fields with respect to location of surface features and to define a range of eddy scales for inhomogeneous fluctuations.

Observations showed MTIBL development on some experimental days (Strunin et al., 2004); a main feature of the MTIBL was the downward sensible heat fluxes that developed over the relatively cold river under unstable thermodynamic conditions. Wavelet cross-scalograms between vertical wind speed and air temperature fluctuations ($w'\theta'$) also reflect this sequence of events (see Figure 2). Cross-scalograms on panels a, b and c, which correspond to 100-, 150- and 300-m flight levels, respectively, show strong downward fluxes over the river lowlands at practically all scales. Cross-scalograms (Figure 2) and vertical cross-sections of sensible heat flux over the Lena River and its

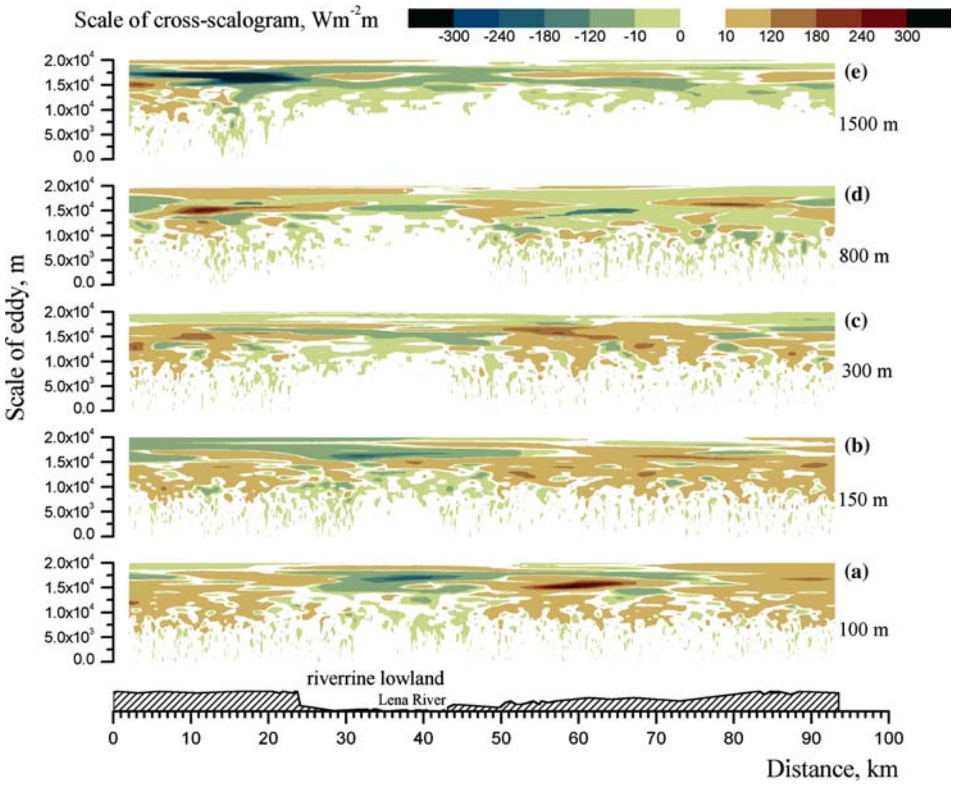

Figure 2. Wavelet cross-scalograms between vertical wind speed w' and potential air temperature θ' (kinematic heat fluxes), obtained at five flight heights from 100 m up to 1500 m (panels a–e) during aircraft experiment on June 19, 2000 over the Lena River and its banks.

lowland (see Figure 4 of Strunin et al., 2004) show good agreement and provide additional observational support for the MTIBL development.

3.2. WAVELET COSPECTRA

Wavelet cospectra between vertical wind speed fluctuations and potential temperature fluctuations $Co_{w\theta}$, humidity fluctuations Co_{wq} and carbon dioxide fluctuations Co_{wC} were calculated using (14). The original time series used in the calculations were not filtered. It is well known that wavelet transforms strongly smooth cospectra at small wavenumbers. This is an important feature that makes wavelet methods very suitable for the spectral analysis of atmospheric turbulence. Cospectra were also smoothed at long wavelengths with a five-point moving average filter. Cospectra were then normalised as $\mathrm{Cn}_{w\theta} = \frac{kCo_{w\theta}}{\overline{(w'\theta')}_0}$, where k is the current wavenumber, and $\overline{(w'\theta')}_0$ is the line-averaged kinematic heat flux at the 100-m flight level. Ground measurements were made only at two points under the aircraft sampling paths (see Figure 1a and b), so ground-based data could not correctly characterise inhomogeneous surface conditions related to CBL development (Strunin et al., 2004). Instead of the corresponding surface data, surface scaling used data at the 100-m flight level, i.e., $(\overline{w'\theta'})_0 = w_*\theta_*$. Scaling errors introduced by using data at the lowest flight level should be smaller than errors introduced by applying point measurements of ground-based fluxes related to quite different dynamic and thermal situations.

The fluxes $(w'C')$ and $(w'q')$ were scaled by the maximum absolute values of the corresponding line-averaged fluxes (i.e., as $\mathrm{Cn}_{wC} = \frac{kCo_{wC}}{|\overline{w'C'}|_{\max}}$ and $\mathrm{Cn}_{wq} = \frac{kCo_{wq}}{|\overline{w'q'}|_{\max}}$, respectively) to compare cospectra. Maximum values $|\overline{w'C'}|_{\max}$ and $|\overline{w'q'}|_{\max}$ were from one of the flight levels between 100 and 1500 m on the corresponding experiment day. Because of the unstable thermal conditions, kinematic fluxes $(\overline{w'\theta'})_0$ were upward and the largest on each of the flight days, i.e., $(\overline{w'\theta'})_0 = |\overline{w'\theta'}|_{\max}$ (see values of fluxes H_0 in Table I). Thus, scaling methods for cospectra $(w'\theta')$, $(w'C')$ and $(w'q')$ were practically the same, because in each case the maximum absolute value of the corresponding flux was used.

Figure 3A-C show plots of normalised wavelet cospectra $\mathrm{Cn}_{w\theta}$, Cn_{wq} and Cn_{wC}, respectively, versus normalised (non-dimensional) wavenumber kz (where z is the current flight level) for flight experiments from 1 May to 19 June. The cospectra demonstrate the relative contribution of eddies at different scales to the total flux. The evolution of the cospectra $\mathrm{Cn}_{w\theta}$ depends on the day of the experiment and the height above the underlying surface. Tracing the evolution reveals the development of the CBL under different thermodynamic and surface conditions. Figure 3A shows that the vertical behaviour of cospectra $\mathrm{Cn}_{w\theta}$ agrees with a generally accepted model for sensible heat flux in the CBL. The cospectral shape and peak magnitudes depend on the relative (normalised) height $\frac{z}{\delta_i}$ above the underlying surface. Cospectra $\mathrm{Cn}_{w\theta}$ for heights of 100–300 m (which correspond to $\frac{z}{\delta_i} \approx 0.1-0.2$) were positive at all eddy scales for all flight days. Largest cospectral magnitudes occurred at the lowest level (100 m, $\frac{z}{\delta_i} \approx 0.1$ or less). Negative cospectra peaks in the longwave part of the range arose only at normalised heights exceeding 0.6; cospectral magnitudes decreased with height. Most cospectra had two clearly expressed peaks, suggesting the existence of exchange mechanisms with two dominant scales. This is not a unique situation. Petrova (1974) reported two-peaked cospectra of vertical wind speed and temperature measured on a 300-m meteorological tower in Obninsk (a city near Moscow, Russia). It is likely that the smaller-scale peak reflects small-scale turbulent motion and the larger-scale peak reflects mesoscale flow. Cospectra became partly negative at the highest flight levels (1500 m and at 800 m for flights on May 9, June 9, and June 19, when $\frac{z}{\delta_i} > 0.6$). This occurred when downward mesoscale sensible heat fluxes appeared. Negative

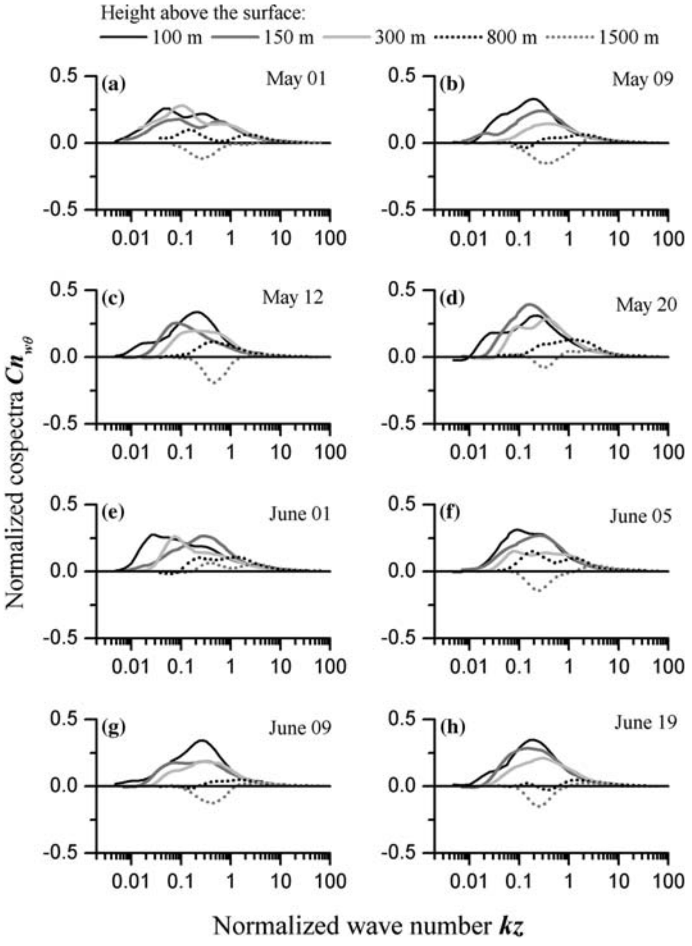

Figure 3. (A) Normalized cospectra $\frac{kCo_{w\theta}}{\overline{(w'\theta')}_0}$ between vertical wind speed w' and potential temperature θ' fluctuations (sensible heat fluxes H) versus the normalized (non-dimensional) wavenumber kz for different days (May 01, 09, 12, 20 and June 01, 05, 09, 19; panels a–h). (B) Same as (A), but for cospectra $\frac{kCo_{wq}}{|\overline{w'q'}|_{\max}}$ (water vapour fluxes E). (C) Same as (A), but for cospectra $\frac{kCo_{wC}}{|\overline{w'C'}|_{\max}}$ (carbon dioxide fluxes Q).

peaks arose only in cospectra obtained for normalised heights $\frac{z}{\delta_i} > 0.6$, a height range which is near the point at which sensible heat flux typically changes from positive to negative. Total flux becomes downward due to negative mesoscale fluxes although small-scale turbulent transport remains upward. This provides an opportunity to examine separately mesoscale and small-scale turbulent motions. Additionally, if the reduced depth of the CBL δ_i is used for height scaling, similarity models of the CBL may be applied to a non-homogeneous structure.

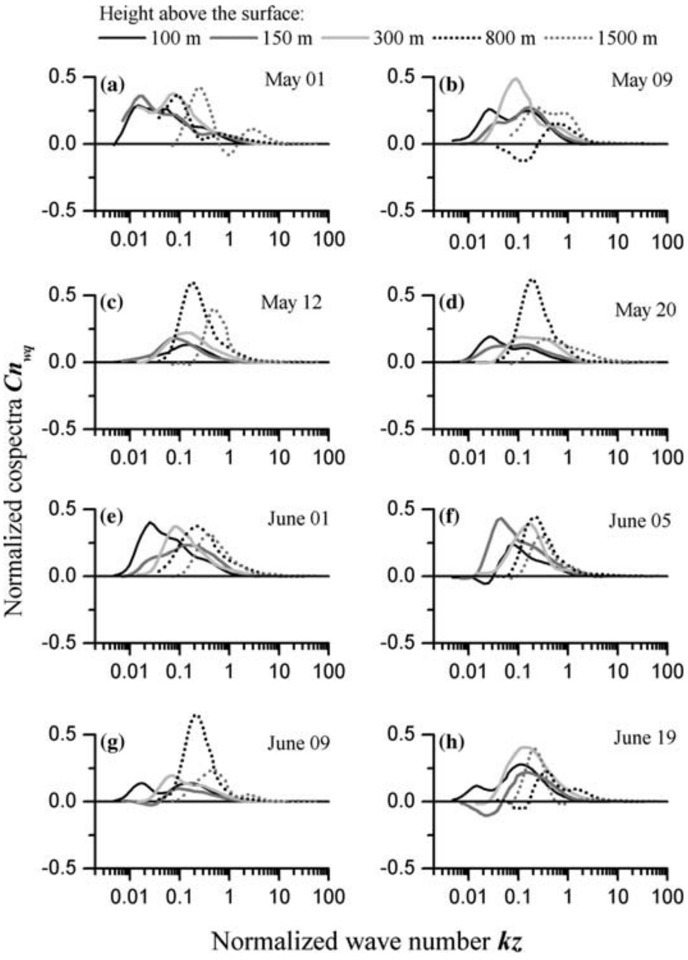

Figure 3B. Continued.

The cospectra Cn_{wq} showed big differences in behaviour (Figure 3B), and large peaks of small-scale turbulent cospectra Cn_{wq} were not present. The strongest water vapour transport was caused mainly by mesoscale eddies. Nevertheless, detailed consideration of the cospectra allowed a separation of small-scale turbulent peaks that were close (in wavenumber space) to mesoscale peaks. The technique used to separate peaks is described below. Maximum water vapour fluxes occurred mainly at 800 m, and in some cases, 300 m (Strunin et al., 2004). This observation agrees with cospectra shown in Figure 3B, in which the maximum cospectral Cn_{wq} values occurred at 800 m, which corresponds to a normalised height $\frac{z}{\delta_i}$ of 0.3–0.5.

Carbon dioxide fluxes depend strongly on sinks and sources at the underlying surface. Cospectra Cn_{wC}, as presented in Figure 3C, clearly

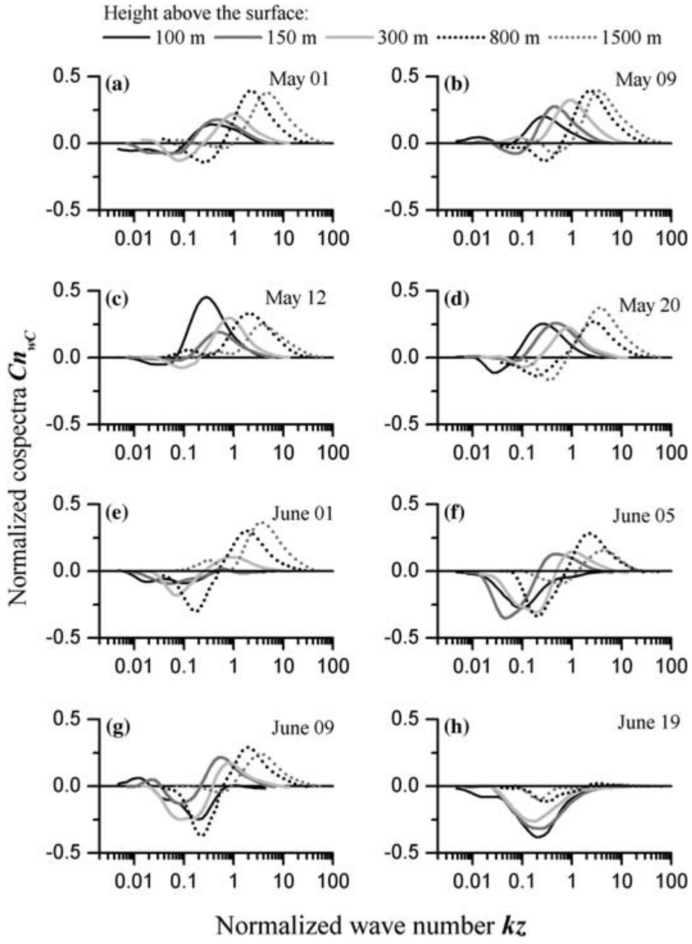

Figure 3C. Continued.

reveal distinctions between mesoscale and small-scale turbulent motions. Negative mesoscale and positive small-scale turbulent parts exist in each cospectrum in most cases. Downward transport of carbon dioxide occurred mainly through mesoscale motions. In contrast, turbulent transport of carbon dioxide was downward only on June 19, a day when the surface was covered with dense, green vegetation that acted as a strong carbon dioxide sink. Otherwise, small-scale turbulent fluxes of Cn_{wC} were upward. The shape and intensity of cospectra for height ranges from 800 to 1500 m (normalised heights of 0.3 to 1.1) were very similar on different observation days. Only the strong surface source of carbon dioxide on May 12 (due to snow melt and the absence of green vegetation cover) and the strong sink on June 19 altered this effect.

3.3. SEPARATING SPECTRA INTO SMALL-SCALE TURBULENT AND MESOSCALE PARTS

Clearly expressed peaks in the cospectra (Figure 3A–C) suggest that two scales of motion induced fluxes in the CBL. The first scale is consistent with small-scale turbulent eddies with scales less than the reduced depth of the CBL δ_i. The second scale is consistent with mesoscale flows with scales ranging from δ_i (about 2 km) up to 20 km. The cospectra can be represented as a combination of two Gaussian curves.

Figure 4 shows the procedure for separating cospectra into small-scale turbulent and mesoscale parts. Four typical situations were considered. Calculated cospectral curves are presented as functions of wavenumber and are shown as the solid black line. Dotted grey lines and solid grey lines respectively represent the small-scale turbulent and mesoscale parts of the cospectrum. In the most distinct case, small-scale turbulent and mesoscale cospectral peaks are far from each other in wavenumber space (scales differ by 5–10 times). The cospectral minimum was chosen to be the boundary between the parts (panel a in Figure 4, boundary shown with the line A–B). This situation was typical for numerous ($w'\theta'$) cospectra. If mesoscale and small-scale turbulent peaks had opposite signs, the point at which the cospectra change sign was considered the boundary between the two motions. For this situation, the peaks could be close to each other (panel b in Figure 4) or far from each other (panel c in Figure 4), but the separation principle is simple. These situations were most typical for cospectra of ($w'C'$).

If cospectral peaks were close to one another in wavenumber space (i.e., the scales differed by less than five, as illustrated in panel d of Figure 4), another separation technique was applied. This technique was required mainly for ($w'q'$) cospectra. A tangent to the cospectrum curve between peaks and inclined 45° to the wavenumber axis was constructed to determine the separation point. The intersection of the tangent line and cospectral curve corresponded to the crossing point of additive Gaussian distributions. This point was assumed to be the separation between small-scale turbulent and mesoscale fluxes.

All cospectra (solid black curves) can therefore be treated as a combination of two independent distributions: the right-hand one (dashed grey) reflects small-scale turbulence, and the left-hand one (solid grey) is consistent with mesoscale flow. Small-scale turbulent and mesoscale fluxes are defined under the dashed and solid grey curves, respectively, by squares (Figure 4, panel a). In practice, it is impossible to extract correctly the additive distributions, but the square under the dashed grey curve (the small-scale turbulent portion of the cospectrum) is approximately equal to the square under the solid black curve to the right of line A–B. Similarly, the square under the solid grey curve (the mesocale part of the cospectrum) is approximately equal to the square under the solid black curve to the left of A–B. The small-scale turbulent flux can

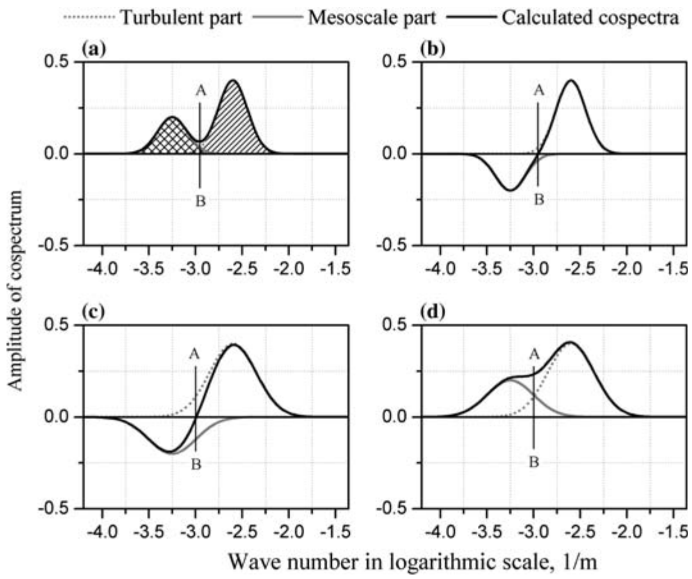

Figure 4. Scheme of separating the mesoscale and small-scale turbulent portions of cospectra for their different combinations: typical situations for cospectra ($w'\theta'$) (panel a), cospectra ($w'C'$) (panels b and c) and for cospectra ($w'q'$) (panel d). Line A–B in panels shows the scale boundaries between mesoscale and turbulent parts of cospectra.

therefore be calculated by integrating the curve to the right of the spectral boundary A–B (the area hatched by diagonal lines in Figure 4, panel a). Similarly, the mesoscale flux results from integrating this curve to the left of the boundary (the cross-hatched area in Figure 4, panel a). Cospectra are thus the superposition of two motions that can be explored separately. Different relationships for small-scale turbulent and mesoscale portions of fluxes can therefore be derived. The boundaries estimated for the cospectra ($w'\theta'$), ($w'C'$) and ($w'q'$) were all nearly the same, which suggests that this method could be useful not only for fluxes, but also for other variables.

3.4. SCALING OF SMALL-SCALE TURBULENT AND MESOSCALE FLUXES AND VARIANCES

Fluxes estimated by integrating the cospectra showed excellent agreement with fluxes calculated by the eddy correlation method (Strunin and Hiyama, 2004a). The line-averaged flux, H_0, which maximised at the 100-m flight level, was applied as a scaling value for modelling vertical sensible heat flux distribution. As noted above, data from the lowest flight level were treated as surface values for scaling. This approach was successful for the mosaic method (Strunin et al., 2004) and for determining normalised cospectra (see Section 3.2).

Section 3.3 noted that maximum water vapour fluxes occurred at different levels between 100 and 1500 m on different observation days. Thus, the line-averaged maximum water vapour flux $E_{\max}$ was used as the reference value for each case. The same scaling scheme was applied to momentum fluxes: the line-averaged maximum (in absolute value) flux $M_{\max}$ from a flight level between 100 and 1500 m was used as the scaling value.

Scaling of carbon dioxide flux based on the surface or lowest flight-level values failed for all cases because the total flux, defined as a sum of the mostly positive small-scale turbulent and mostly negative mesoscale fluxes, could be close to zero at this level (see panel c in Figure 4). Instead, the absolute value of the maximum flux $|Q_{\max}|$ that occurred in the observations between 100 and 1500 m was used to scale carbon dioxide flux. The mesoscale and small-scale turbulent parts of the fluxes were of opposite sign in many cases, so the maximum value of the flux was defined as the sum of the absolute values of the small-scale turbulent $|Q_{T\max}|$ and mesoscale $|Q_{M\max}|$ parts: $|Q_{\max}| = |Q_{T\max}| + |Q_{M\max}|$. A detailed analysis of carbon dioxide flux distribution revealed similarities in individual vertical profiles for the different observation days. This similarity existed in both small-scale turbulent and mesoscale portions of the fluxes. The main difference between the profiles was a shift that occurred along the flux amplitude axis; the shift can be defined as the vertical average flux Q_{av}. Thus, both small-scale turbulent and mesoscale parts of the fluxes can be scaled as $\frac{Q-Q_{av}}{|Q_{\max}|}$, where Q_{av} was determined by averaging small-scale turbulent and mesoscale portions of fluxes separately in the air column over the sampling site.

Figure 5 presents results of flux scaling based on data obtained for all regional sampling paths (experiments from May 1 to June 19, 2000). Table I includes scaling values of fluxes H_0, $M_{\max}$, $E_{\max}$ and $|Q_{\max}|$. Height was normalised by the corresponding reduced depths of the CBL δ_i (see Table I). The figure also includes typical values for the 90% confidence intervals for the random error (see Section 2.3.1).

Figure 5 shows different behaviour for small-scale turbulent and mesoscale flux profiles. Small-scale turbulent sensible heat fluxes rapidly and monotonically decreased with height and became negligibly small near the upper boundary of the CBL (marked on the left-hand side panels by dashed lines at the $\frac{z}{\delta_i} = 1$ level). Scatter is very small (even smaller than typical scatter in generally accepted similarity models). Scatter in small-scale turbulent fluxes of normalised momentum and water vapour was larger, but these fluxes also decreased with height and became small at the top of the CBL (normalised height $\frac{z}{\delta_i} = 1$). In no case did scatter in the profile exceed the 90% confidence intervals. Small-scale turbulent carbon dioxide fluxes can be upward or downward depending on surface conditions. In addition, the average value, which is used to shift the flux scaling, changes noticeably. However,

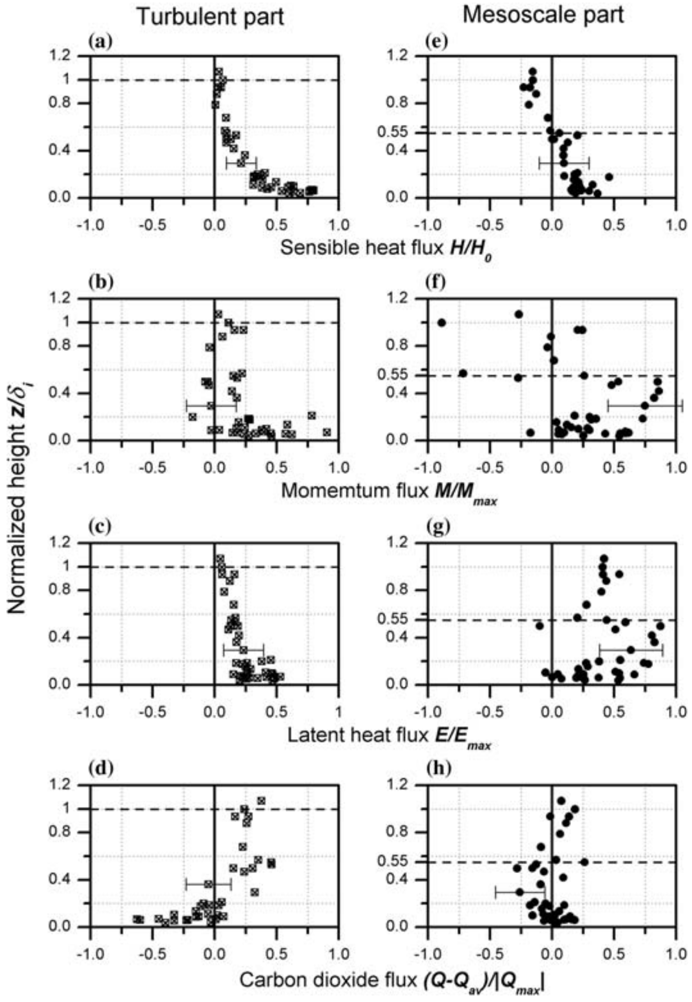

Figure 5. Scaling of small-scale turbulent (panels a, b, c and d), and mesoscale parts (panels e, f, g and h) of sensible heat H, momentum M, water vapour E and carbon dioxide Q fluxes based on correspondent absolute maximum fluxes. Typical confidential intervals for small-scale turbulent and mesoscale part of the fluxes are also shown.

the shape of the scaled flux profile resembles those for other small-scale turbulent fluxes. Thus, small-scale turbulent carbon dioxide flux behaviour is analogous to other small-scale turbulent fluxes, but modified by the non-zero flux reference value.

Vertical profiles of mesoscale fluxes (right-hand side panels in Figure 5) differ considerably from the corresponding turbulent fluxes. All profiles changed behaviour at the same normalised height $\frac{z}{\delta_i} \approx 0.55$ (marked by dashed lines in the right-hand side panels of Figure 5). This inflection exceeds the 90% confidence interval and can be treated as significant. Sensible heat fluxes were almost constant up to this height and had values of 0.2–0.4 of the total fluxes. However, above $\frac{z}{\delta_i} > 0.55$, fluxes decreased rapidly and became negative (downward flux) at normalised heights of 0.7–0.8. The profile of mesoscale fluxes of water vapour also changed behaviour at the normalised height of 0.55. The scatter for the momentum flux profile is larger, but a similar change exists at the same relative height. Finally, the behaviour of the carbon dioxide mesoscale profile resembles the other mesoscale fluxes.

Single variables, such as horizontal and vertical wind speed fluctuations and air temperature fluctuations, were also scaled to separate small-scale turbulent and mesoscale parts of variances according to scale boundaries defined for the fluxes on the corresponding flight paths. The scaling values used were convective velocity (Equation (6)) and convective temperature (Equation (7)) estimated for the total flight path at the 100-m level for each regional flight. Height was scaled using the reduced depth of the CBL δ_i. Figure 6 shows scaling results for wind speed and air temperature fluctuations.

The three top panels (Figure 6a, c and e) show the scaling of the small-scale turbulent portions of variances; dashed lines denote the upper boundary of δ_i. Scatter was rather small, and the profiles can be fitted with smoothed curves, as are usually applied to the homogeneous CBL. The following relations are derived for the small-scale turbulent part of fluctuations to fit the profile of horizontal wind speed variances:

$$\frac{\sigma_u^2}{w_*^2} = 0.15\left(\frac{z}{\delta_i}\right)^{4/3}\left(1 - 0.9\frac{z}{\delta_i}\right)^{2/3} + 0.015\left(\frac{z}{\delta_i}\right)^{-2/3}\left(1 - 0.9\frac{z}{\delta_i}\right)^{2/3}, \tag{17}$$

and to fit vertical wind speed variances,

$$\frac{\sigma_w^2}{w_*^2} = 0.6\left(\frac{z}{\delta_i}\right)^{2/3}\left(1 - 0.8\frac{z}{\delta_i}\right)^{2}. \tag{18}$$

Equation (18) resembles that commonly used for a homogeneous CBL (Stull, 1988; Kaimal and Finnigan, 1994) and for mosaic segments with a relatively homogeneous mixed layer structure (Strunin et al., 2004). The only difference is the numerical coefficient, which is a third of that used for the homogeneous case. The relation for the potential temperature variances was of a form suggested by Sorbjan (1991):

$$\frac{\sigma_\theta^2}{\theta_*^2} = 0.4\left(\frac{z}{\delta_i}\right)^{-2/3}\left(1 - \frac{z}{\delta_i}\right)^{4/3} + 0.4\left(\frac{z}{\delta_i}\right)^{4/3}\left(1 - \frac{z}{\delta_i}\right)^{-2/3}. \tag{19}$$

Numerical coefficients in Equation (19) are also a fraction of the coefficients for the homogeneous cases. Such smaller coefficients appear after excluding mesoscale eddies from consideration.

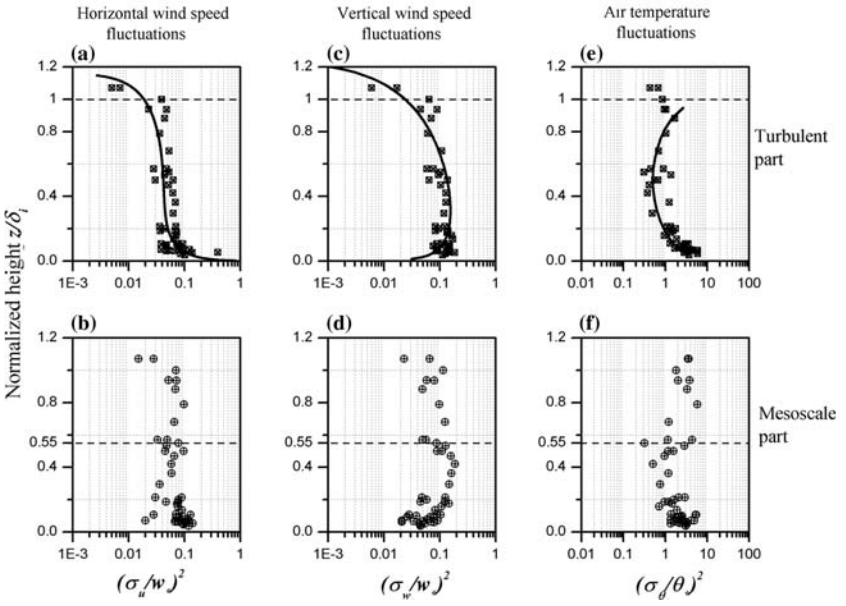

Figure 6. Scaling the small-scale turbulent and mesoscale parts of horizontal (panels a and b) and vertical (panels c and d) wind speed fluctuations and air temperature fluctuations (panels e and f).

The three bottom panels in Figure 6 present the scaling of the same variations, but in the mesoscale. Dashed lines show the 0.55 levels, where the flux profiles change behaviour as noted above. The figure shows that profiles of normalised mesoscale variances also change behaviour in the same manner at the same level (0.55).

3.5. Coherence of fluctuations

Coherence between vertical wind speed fluctuations and fluctuations in horizontal wind speed, potential temperature, air humidity, and of carbon dioxide density were calculated using (16). Coherence had peaks at small-scale turbulent and mesoscale wavenumbers that matched peaks in the cospectra. The coherence spectra can be separated into small-scale turbulent and mesoscale parts using the same scale boundaries as for the fluxes.

Application of the separation approach to the coherence spectra allowed an estimation of correlations between parameters at different scales. Coherences were averaged for wavenumber intervals corresponding to turbulent and mesoscale motions; these were the coherence between parameters with small-scale turbulent and mesoscale ranges, respectively. Figure 7 shows vertical profiles of coherence between fluctuations u' and w', w' and θ', w' and C', and w' and q' for small-scale and mesoscale motions.

Coherence profiles resembled the corresponding small-scale turbulent flux distributions. Coherences of $(u'w')$, $(w'q')$ and $(w'\theta')$ calculated for the smaller scales of the spectra decreased rapidly and monotonically with height. Coherences of $(u'w')$ and $(w'q')$ were small at all heights and did not exceed 0.1 at the lowest levels. Correlation between u' and w' and between w' and q' vanished at the top of the CBL. Coherence $(w'\theta')$ showed larger values (about 0.3 at the lowest level) but also decreased with height. Correlation between w' and θ' was low only at the top of the CBL.

The behaviour of coherence between small-scale turbulent fluctuations of w' and C' differed from the other turbulent variables. The coherence profile of $(w'C')$ was a maximum, about 0.3–0.4, in the middle of the CBL. The correlation between w' and C' was much greater than that between w' and θ', w' and q', and u' and w'. In all cases, correlation between small-scale turbulent variables approached zero at the top of the CBL.

Figure 7 also shows the coherence distribution for the mesoscale portion of the spectral range (solid circles). Fluctuations of mesoscale variables correlated much better than did those of turbulent variables. Maximum values of

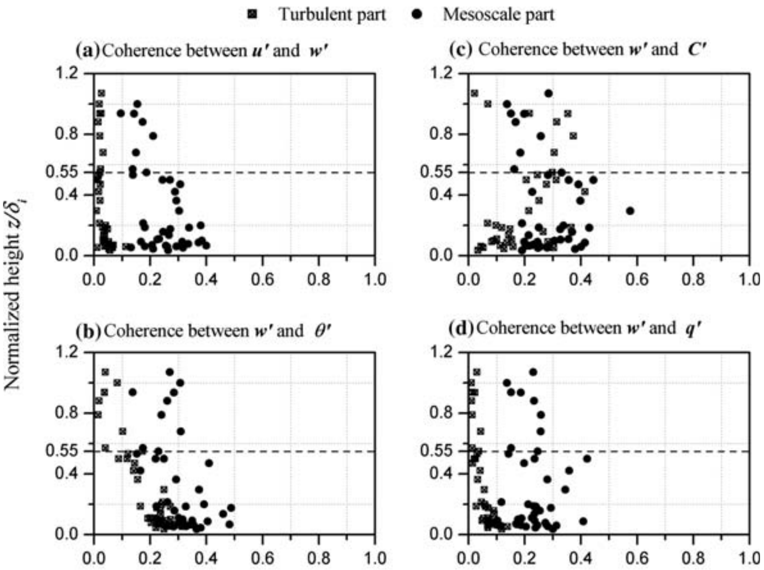

Figure 7. Vertical distribution (profiles) of coherence between vertical wind speed w' and horizontal wind speed fluctuations u' (panel a), potential temperature fluctuations θ' (panel b), fluctuations of carbon dioxide density C' (panel c), absolute humidity fluctuations q' (panel d), calculated for small-scale turbulent and mesoscale parts of scale range.

coherence reached magnitudes of 0.4–0.5 (correlation coefficients 0.6–0.7). These values suggest that mesoscale motions can be treated as so-called ‘coherent structures’, noting that the transport of heat and other substances by coherent structures can be large (see, for example, MacPherson and Betts, 1997). Profiles of the mesoscale part of coherence show sharp inflections at the same normalised height $\frac{z}{\delta_i} \approx 0.55$ as noted in the flux profiles. The inflection appeared in all coherence profiles at the same normalised height, indicating that the same eddies transported both active and passive substances.

3.6. ANISOTROPY OF WIND SPEED FLUCTUATIONS

An important aspect of CBL motion is the isotropy (or anisotropy) of wind speed fluctuations. If a natural boundary exists, the underlying surface will destroy the isotropy of the eddies. Observations of atmospheric turbulent flows have shown that wind speed fluctuations do not obey local isotropy laws (Reiter and Burns, 1966; Vinnichenko et al., 1980). A criterion for estimating turbulence isotropy relates the energy spectra of vertical (S_w) and horizontal (S_u) wind speed fluctuations, or so-called degree of anisotropy:

$$an = \frac{S_w}{S_u}. \tag{20}$$

For local isotropic inertial subrange turbulence, the theoretical value of *an* is 4/3 (Monin and Yaglom, 1971). The vertical temperature stratification, horizontal advection, and boundary surfaces all limit the isotropy of atmospheric turbulence. Kaimal et al. (1972) showed that Equation (20) in the surface layer depends on thermal stability and the scale of eddies.

As before, a separation approach was applied to the analysis of the small-scale turbulent and mesoscale parts of the degree of anisotropy. Boundaries between the portions of cospectra as defined earlier were used. Values of *an* were averaged for small-scale turbulent and mesoscale parts of the scale range; errors in *an* were based on the stability of the vertical and horizontal wind-speed wavelet spectra. Spectra were evaluated with a χ^2-distribution (Vinnichenko et al., 1980) separately for the small-scale turbulent and mesoscale parts of the scale range. Subsequently, 90% confidence intervals for *an* were calculated. Figure 8 presents the scaling results for the degree of anisotropy, and includes typical 90% confidence intervals for small-scale turbulent and mesoscale parts of *an*.

At the lowest levels, where the normalised height $\frac{z}{\delta_i} < 0.2$, the degree of anisotropy for small-scale turbulent eddies (panel a) increases with height from values of 1–1.2 to 2–2.5. This increase exceeded typical confidence intervals and scatter and was thus assumed to be a real change. Where $\frac{z}{\delta_i} > 0.2$, scatter was small, the degree of anisotropy was almost constant and $an \approx 1.75$. Note that

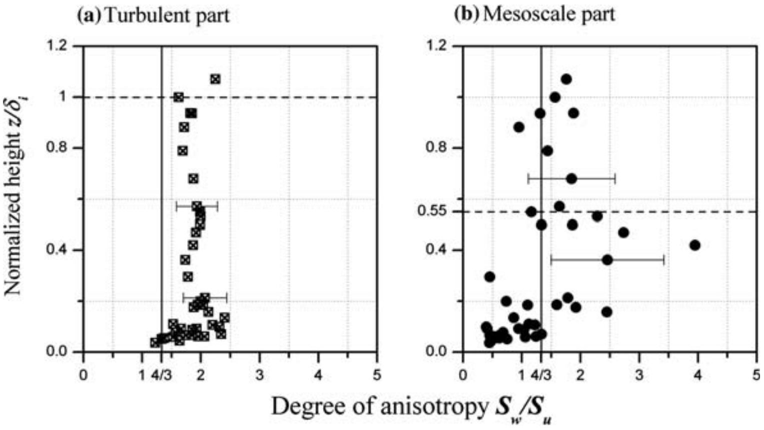

Figure 8. Vertical distribution (profiles) of anisotropy degree $\frac{S_w}{S_u}$ for small-scale turbulent (panel a) and mesoscale (panel b) parts of scale range. Typical confidential intervals are also shown separately for small-scale turbulent and mesoscale ranges.

even the left ends of the confidence intervals exceeded the theoretical value for isotropic turbulence (4/3), marked in the figure by a solid vertical line. This suggests that small-scale turbulent vertical wind speed fluctuations dominated horizontal fluctuations in the mixed layer. This is typical for unstable situations. Aircraft investigations of anisotropy in and around clouds (Strunin, 1990) showed that *an* depends strongly on cloud type and, therefore, on thermodynamic conditions. For example, peaks in *an* for cumulus clouds also exceeded 4/3.

The behaviour of anisotropy for mesoscale fluctuations was quite different. Profiles of *an* were similar to mesoscale profiles of others variables. The profile changed behaviour at the normalised height of approximately $\frac{z}{\delta_i} \approx 0.55$. Below normalised heights of 0.55, values of *an* increased with height from 0.5 to 2.5–4; the corresponding confidence interval was considerably less than this increase. At the lowest levels (where $\frac{z}{\delta_i} < 0.2$), mesoscale horizontal wind speed fluctuations dominated over vertical wind speed fluctuations, but at higher levels the situation reversed. At levels above $\frac{z}{\delta_i} \approx 0.55$, the degree of anisotropy was nearly constant; scatter did not exceed corresponding confidence intervals. Values of *an* were close to the theoretical value of 4/3 (the solid vertical line in panel b of the figure).

4. Conclusion

An aircraft made mean field and turbulent observations along a regional flight path about 90 km in length, and a wavelet transform was applied to the observations to determine turbulent fluxes over a thermally well-marked mesoscale heterogeneous land surface. The flight distance supported analysis of atmospheric eddies with a maximum size of 20 km. Figure 3A–C showed that cospectra had small power at scales close to 20 km. In addition, cospectral values decreased in the right-hand, small-scale part of the wavenumber range. Thus, the obtained cospectra fully overlap the scale range of fluctuations observed in the CBL. This was also corroborated by direct comparison of fluxes calculated using cospectra and using the eddy correlation method (Strunin and Hiyama, 2004a).

Cospectra obtained within a mixed layer that develops over a homogeneous land surface usually have only one maximum (or minimum) and have the same sign at different scales (see, for example, Desjardins et al., 1989, 1997). Observations in the present study occurred over thermally non-homogenous terrain; typical scales of surface heterogeneity exceeded Raupach's length, so no known similarity model can be applied to scale the CBL. Obtained cospectra in Figure 3A–C show distinct expressed peaks in different wavenumber ranges, which were distinctly separated in wavenumber space. That separation permits a division of the flows into small-scale turbulent and mesoscale portions. The boundary between the small-scale turbulent and mesoscale flow varied in a narrow range between 1000 and 1700 m, which is close to the reduced depth of the CBL δ_i. The scale boundaries, which were defined through cospectra according to the schemes in Figure 4, were useful for separating the spectra of single variables. This approach (named the 'separation approach') allowed construction of similarity models of fluxes and other variables for given thermodynamic and surface conditions. This is similar to Kaimal's (1978) suggestion that spectra of horizontal wind speed fluctuations can be separated into low frequency 'convective' and high frequency 'mechanical' portions with a boundary of spectra scale z_i.

Peaks in the spectra of coherence and in the spectra of single variables correspond to the cospectral peaks. Table II presents scales of motions and corresponding peaks in cospectra and the degree of anisotropy using absolute l and normalised $\frac{l}{\delta_i}$ scale lengths. Table II shows that small-scale turbulent and mesoscale eddy scales differed by a factor of 5–10; averaged scales, as defined by different variables' distributions, were close to each other for both small-scale turbulent and mesoscale ranges.

The separation approach revealed different behaviours of variables in different scale ranges. These differences are distinct in the vertical flux distributions (Figure 5), profiles of normalised variations (Figure 6), coherence profiles (Figure 7) and the degree of anisotropy vertical distributions (Figure 8). The magnitude of small-scale turbulent fluxes, coherence and degree of anisotropy decreased rapidly and monotonically with height above the land surface (except for the carbon dioxide small-scale turbulent flux and the coherence between w' and C'), becoming negligibly small at the top of the CBL. Vertical distributions of small-scale turbulent fluxes are determined

TABLE II

Turbulent and mesoscale scales defined based on different kinds of fluxes and degree of anisotropy relation.

	Momentum flux		Sensible heat flux		Water vapour flux		Carbon dioxide flux		Degree of anisotropy	
	Turbulent	Mesoscale	Turbulent	Mesoscale	Turbulent	Mesoscale	Turbulent	Mesoscale	Turbulent	Mesoscale
l, m	550	4300	650	3800	850	4550	400	3900	380	3950
$\frac{l}{\delta_i}$	0.30	2.40	0.32	2.20	0.43	2.62	0.23	2.29	0.21	2.31

l: is the mean size of turbulent and mesoscale eddies;
$\frac{l}{\delta_i}$: is the mean normalised scale of turbulent and mesoscale eddies.

by surface conditions, whose influence extends nearly to the top of the CBL but undergoes strong decay.

Strong decay of small-scale turbulent sensible heat fluxes contradicts generally accepted similarity models of the CBL (see, for example, Sorbjan, 1991; Kaimal and Finnigan, 1994). Figure 5 shows that total sensible heat flux profiles could be estimated by summing the small-scale turbulent and mesoscale portions of the fluxes. The summed profile has a shape close to that arising from the conventional similarity model. The flux decreased with height, vanished at a normalised height $\frac{z}{\delta_i} \approx 0.7$–$0.8$ and became negative at higher levels. This is similar to a conventional model of the flux profile in the CBL over a homogeneous land surface. However, a more detailed investigation shows that the sensible heat flux profile does not strictly obey the generally accepted model. The profile bends at a normalised height of 0.1–0.2 (because of large values of small-scale turbulent flux) and again at a height of 0.5–0.6 (where a strong inflection occurs in the mesoscale flux profiles). Albertson and Parlange (1999) predicted this shape to the sensible heat flux profile over an arid heterogeneous patchy surface using a large-eddy simulation (see Figure 2 in Albertson and Parlange, 1999).

In contrast to the other profiles, the scaled profile of carbon dioxide small-scale turbulent flux (see Figure 5) approaches non-zero values with increasing normalised height. Although the shape of the flux profile is similar to all other turbulent flux profiles, the small-scale turbulent flux of carbon dioxide did not vanish to the top of the CBL.

All profiles of mesoscale variables are characterised by a similar inflection at the same normalised height ($\frac{z}{\delta_i} \approx 0.55$); this inflection is distinct in all mesoscale flux distributions, degree of anisotropy, variances of wind speed and temperature fluctuations and coherence. The magnitude of the inflection in all cases exceeds the 90% confidence intervals.

In contrast to the cospectra and fluxes, the degree of anisotropy was estimated based on the independent wavelet spectra of S_w and S_u. However, the degree of anisotropy profile has an inflection at the same relative level as other variables, indicating that the same eddies control mesoscale motion of both active and passive substances.

Mesoscale flows in the upper and lower parts of the CBL have a different nature. The impact of mesoscale motion increases with height and maximises in the middle part of the mixed layer. Mesoscale exchanges then sharply decrease, but increase again at higher levels. This behaviour reflects two mechanisms affecting mesoscale exchange in the non-homogeneous CBL. One is associated with the influence of a thermally heterogeneous land surface, an influence that extends up to the middle of the CBL ($\frac{z}{\delta_i} \approx 0.55$); the second is related to entrainment between the CBL and the free atmosphere or, in the case of MTIBL development, entrainment between the upper part of the layer and zones above that layer. Thus, the present study suggests that the influence of surface-level thermal mesoscale heterogeneity extended only up to the normalised height of $\frac{z}{\delta_i} \approx 0.55$. The next loop in the vertical profile is determined by entrainment from the free atmosphere (if no MTIBL develops) or from the zone above the MTIBL (if one develops). The region above the MTIBL development should be treated as an area of entrainment (Strunin et al., 2004) rather than free atmosphere.

Acknowledgements

The authors thank Prof. T. Yasunari of Nagoya University, Japan, Prof. Y. Fukushima of the Research Institute for Humanity and Nature, Japan, and Prof. T. Ohata of the Frontier Observational Research System for Global Change, Japan. Without their efforts and leadership, the aircraft observations would not have been possible. Thanks are also due to all members of the aircraft team and the GAME-Siberia scientific team for the aircraft-based and tower-based turbulence measurements. This research was financially supported, in part, by a grant from the Frontier Observational Research System for Global Change (FORSGC), Japan, and by the Ministry of Education, Culture, Sports, Science and Technology of Japan (grants no. 11201206 and no. 12460063).

References

Albertson, J. D. and Parlange, M. B.: 1999, 'Natural Integration of Scalar Fluxes from Complex Terrain', *Adv. Water Resour.* **23**, 239–252.

Attie, J.-L. and Durand, P.: 2003, 'Conditional Wavelet Technique Applied to Aircraft Data Measured in Thermal Internal Boundary Layer during Sea-breeze Events', *Boundary-Layer Meteorol.* **106**, 359–382.

Brutsaert, W. H.: 1982, '*Evaporation into the Atmosphere*', D. Reidel, Dordrecht, 299 pp.

Deardorff, J. W.: 1970, 'Convective Velocity and Temperature Scale for the Unstable Planetary Boundary Layer and for Rayleigh Convection', *J. Atmos. Sci.* **27**, 1212–1213.

Desjardins, R. L., MacPherson, J. I., Schuepp, P. H. and Karanja, F.: 1989, 'An evaluation of aircraft flux measurements of CO_2, water vapor and sensible heat', *Boundary-Layer Meteorol.* **47**, 55–69.

Desjardins, R. L., MacPherson, J. I., Mahrt, L., Schuepp, P. H., Pattey, E., Neumann, H., Baldocchi, D., Wofsy, S., Fitzjarrald, D., McCaughey, H., and Joiner, D. W.: 1997, Scaling up flux measurements for the boreal forest using aircraft-tower observations', *J. Geophys. Res.* **102**, D24, 29,125–29,133.

Flandrin, P.: 1988, 'Time-frequency and Time-scale', *Proceedings of IEEE Fourth Annual ASSP Workshop on Spectrum Estimation and Modeling*, Minneapolis, Minnesota, pp. 77–80.

Grossman, A. and Morlet, J.: 1984, 'Decomposition of Hardy functions into square integrable wavelets of constant shape', *SIAM J. Math. Anal.* **15**, 723–736.

Hiyama, T., Strunin, M.A., Suzuki, R., Asanuma, J., Mezrin, M.Y., Bezrukova, N.A. and Ohata, T.: 2003, 'Aircraft Observations of the Atmospheric Boundary Layer over a Heterogeneous Surface in Eastern Siberia', *Hydrol. Proc.* **17**, 2885–2911.

Hojstrup, J.: 1982, 'Velocity Spectra in the Unstable Boundary Layer', *J. Atmos. Sci.* **39**, 2239–2248.

Hudgins, L. H., Mayer, M. E. and Frieche, C. A.: 1993, 'Fourier and Wavelet Analysis of Atmospheric Turbulence', in Y. Meyer and S. Roques (eds.), *Progress in Wavelet Analysis and Applications*, Editions Frontiers, pp. 491–498.

Kaimal, J. C.: 1978, 'Horizontal Velocity Spectra in an Unstable Surface Layer', *J. Atmos. Sci.* **35**, 18–24.

Kaimal, J. C. and Finnigan, J. J.: 1994, *Atmospheric Boundary Layer Flows, Their Structure and Measurements,* Oxford University Press, Oxford, 289 pp.

Kaimal, J. C., Wyngaard, J. C. and Izumi, Y.: 1972, 'Spectral Characteristics of Surface-layer Turbulence', *Quart. J. Roy. Meteorol. Soc.* **98**, 563–589.

Kumar, P. and Foufoula-Georgiou, E.: 1994, 'Wavelet Analysis in Geophysics: An Introduction', in *Wavelet in Geophysics*, Academic Press, Inc. pp. 1–43.

Lenschow, D. H.: 1972, '*The Measurements of Air Velocity and Temperature Using the NCAR Buffalo Aircraft Measuring System*', Technical Note TN/STR-74, NCAR, Boulder, Colo, 39 pp.

Lenschow, D. H. and Stankov, B. B.: 1986, 'Length Scale in the Convective Boundary Layer', *J. Atmos. Sci.* **43**, 1198–1209.

Lenschow, D. H., Mann, J. and Kristensen, L.: 1994, 'How Long is Long Enough When Measuring Fluxes and Other Turbulence Statistics', *J. Atmos. Oceanic Technol.* **11**, 661–673.

Lui, P. C.: 1994, 'Wavelet Spectrum Analysis and Ocean Wind Waves', in *Wavelet in Geophysics*, Academic Press, Inc. pp. 151–166.

MacPherson J. I. and Betts A. K.: 1997, 'Aircraft Encounters with Strong Coherent Vortices over the Boreal Forest', *J. Geophys. Res.* **102**, D24, 29,231–29,234.

Mahrt, L.: 2000, 'Surface Heterogeneity and Vertical Structure of the Boundary Layer', *Boundary-Layer Meteorol.* **96**, 33–62.

Mann, J. and Lenschow, D. H.: 1994, 'Errors in Airborne Flux Measurements', *J. Geophys. Res.* **99**, D7, 14,519–14,526.

Mezrin, M. Y.: 1997, 'Humidity Measurements From Aircraft', *Atmos. Res.* **44**, 53–59.

Monin, A. S. and Yaglom, A. M.: 1971, 'Statistical Fluid Mechanics: Mechanics of Turbulence', in J. L. Lumley (Ed.), *English translation,* 1 MIT Press, Cambrige, MA, 789 pp.

Petrova, L. I.: 1974, 'Turbulent Heat and Momentum Fluxes in the Lower 300-m Atmospheric Layer under Convection', *Trydu GGO* **6**(44), 57–68 (in Russian, English résumé).

Reiter, E. R. and Burns, A.: 1966, 'The Structure of Clear-air Turbulence derived from "Topcat" Aircraft Measurements', *J. Atmos. Sci.* **23**, 2.

Sorbjan, Z.: 1991, 'Evaluation of Local Similarity Functions in the Convective Boundary Layer', *Boundary-Layer Meteorol.* **30**, 1565–1583.

Strunin, M. A.: 1990, 'Anisotropy of Wind Speed Pulses in Cloudy Atmosphere', *Sov. Meteorol. Hydrol* **6**, 28–35 (Allerton Press, Inc).

Strunin, M. A.: 1997, 'Meteorological Potential for Contamination of Arctic Troposphere: Aircraft Measuring System for Atmospheric Turbulence and Methods for Calculations its Characteristics. Archive and Database of Atmospheric Turbulence', *Atmos. Res.* **44**, 17–35.

Strunin, M. A., Hiyama, T., Asanuma, J. and Ohata, T.: 2004, 'Aircraft Observations of the Development of Thermal Internal Boundary Layers and Scaling of the Convective Boundary Layer over Non-homogeneous Land Surfaces', *Boundary-Layer Meteorol.* **111**, 491–522.

Strunin, M. A. and Hiyama, T.: 2004a, 'Applying Wavelet Transforms to Analyse Aircraft-measured Turbulence and Turbulent Fluxes in the Atmospheric Boundary Layer over Eastern Siberia', *Hydrol. Proc.* **18**, 3081–3098.

Strunin, M. A. and Hiyama, T.: 2004b, 'Response Properties of Atmospheric Turbulence Measurement Instruments using Russian Research Aircraft', *Hydrol. Proc.* **18**, 3099–3117.

Stull, R. B.: 1988, *An Introduction to Boundary Layer Meteorology,* Kluwer Academic Publishers, Dordrecht, 666 pp.

Vinnichenko, V. K., Pinus, N. Z., Shmeter, S. M. and Shur, G. N.: 1980, *Turbulence in Free Atmosphere,* Consultants Bureau, New York, 310 pp.

Walker, J. S.: 1997, 'Fourier analysis and wavelet analysis', *Notices Amer. Math. Soc.* **44**, 658.

Wyngaard, J. C.: 1973, 'On Surface Layer Turbulence', in D. A. Haugen (ed.), *Workshop on Micrometeorology,* Boston MA, Amer. Meteorol. Soc., pp. 101–149.